Tensile behavior of hexagonal rare-earth-based low, medium, and high entropy alloys: Strengthening effect of configurational entropy

Laura Rosenkranz[1], Michael Feuerbacher[2], Christian Gadelmeier[1], Felix Schleifer[1] and Uwe Glatzel[1]*

[1]Metals and Alloys, University of Bayreuth, 95447 Bayreuth, Germany

[2] Ernst Ruska-Centre for Microscopy and Spectroscopy with Electrons, Forschungszentrum Jülich GmbH, D-52428 Jülich, Germany

corresponding author: *uwe.glatzel@uni-bayreuth.de

Abstract

In the equiatomic hexagonal close packed high entropy alloy Ho-Dy-Y-Gd-Tb, there is a discrepancy, called the Gibbs paradox, between the extraordinary similarity of the constituent rare earth elements and its calculated configurational entropy. Equiatomic alloys made from one to five rare earth elements, with varying configurational entropy, are investigated for this work to evaluate this paradox in the context of tensile behavior. Assuming comparable microstructures and minimized solid solution strengthening due to the similarity of the constituent elements, a possible strengthening effect of the high configurational entropy is assessed. The alloys are successfully prepared via arc melting with comparable grain sizes and near equiatomic compositions. X-Ray diffraction, and elemental mappings with energy-dispersive X-Ray spectroscopy indicate single-phase microstructures in all alloys except for Ho-Y and Ho-Y-Gd. Tensile tests at room temperature show that the tensile strength of the single-phase alloys lies in the range of the pure elements, which confirms the hypothesis of minimized solid solution strengthening. Those alloys containing additional phases as well as the high entropy alloy show pronounced brittle behavior. No direct correlation between tensile behavior at room temperature and configurational entropy is observed. We state that this alloy system is a suitable candidate for evaluating the Gibbs paradox and disproving an entropy effect on the tensile behavior of this alloy system. This work contributes to understanding mechanical properties and the influence of configurational entropy on the hexagonal close packed high entropy alloy Ho-Dy-Y-Gd-Tb.

Keywords:

A high entropy alloys; B solid-solution hardening; C casting; D microstructure; F mechanical testing

1. Introduction

Research on high entropy alloys (HEA) meets the demand for increasingly high-performance materials and enables the investigation of fundamental concepts in material science. The key concept of HEA is to create solid solutions from at least five alloying elements (5 - 35 at.%) with equiatomic composition and thus without a main alloy element [1-4]. These alloys show chemical disorders with simple crystal structures formed simultaneously, and it is hypothesized that they possess high phase stability up to their melting temperatures without the formation of intermetallic phases [3,5,6]. HEA are reported to exhibit superior properties in strength and ductility, magnetism, resistance against oxidation, and wear compared to conventional alloys [6–8].

Conventional alloys based on a single element have been researched and applied for decades. In contrast, little is known about the HEA formation of HEA, the existence range of which is located in the center of a multi-dimensional phase diagram [9,10]. A multitude of possible, promising alloy compositions is opposed by little data on material properties [1,7]. Conventional theories on alloy formation, e.g., the "solute-solvent" principle, are not necessarily applicable without a base element [8], so new concepts are currently being developed. Four core effects of HEA that influence the microstructure and properties have been proposed: a high entropy effect, severe lattice distortion effect, sluggish diffusion effect, and cocktail effect [4,7,9-11]. HEA's high configurational entropy ΔS_{conf} was suggested to stabilize single-phased solid solution materials [7,8,12].

Although computer-aided efforts are being made to identify promising single-phase alloy candidates [13,14], up to now, most researched materials with high ΔS_{conf} do not stabilize as single-phase solid solutions [8]. Despite excessive research, the suggested four core effects were only partly confirmed experimentally in individual cases [5,15]. Hence, the relevance of the high entropy effect on microstructure and the resulting properties of HEA is currently being questioned [3]. The underlying relations between microstructure and the resulting properties of HEA mostly remain unknown [16]. Recent research focuses on HEA that form single-phase solid solutions, with a large amount of research on the Cantor alloy Cr-Mn-Fe-Co-Ni (20 at.% per element) [1,17]. This approach offers the observation of fundamental material behavior independent of additional effects of secondary phases [3].

The main emphasis of the current HEA research was on face-centered cubic (fcc), e.g., Cantor alloy, and body-centered cubic (bcc), e.g., Senkov alloy, HEA and only a minor proportion of HEA research has been dedicated to hexagonal-close-packed (hcp) materials [15-17]. One of the single-phase hcp HEA found is the rare-earth-based equiatomic alloy Ho-Dy-Y-Gd-Tb. It was first described by Feuerbacher et al., and this alloy forms a magnesium-type solid solution [17]. In this contribution, we will name Ho-Dy-Y-Gd-Tb as HEA-Fb with Fb for Feuerbacher. HEA-Fb consists of rare earth elements with remarkably high similarities in their chemical and physical properties, e.g., atomic radius, density, and melting temperatures. All constituent elements exhibit a hexagonal lattice

structure with P63/mmc space group and 4f electronic configuration [18]. Due to the lanthanide contraction, the differences between covalent atomic radii are less than 3.2 %, and the differences between ionic atomic radii are less than 4.3 %. As ionic radii determine the chemical behavior, the rare earth elements provide a HEA with minimized differences between its elements [18-22].

For comparison: the maximum differences in the atomic radii within the Cantor alloy are 13 % for the covalent atomic radii and more than 28 % for the ionic atomic radii [23]. Previous contributions investigate lattice parameters, microstructure, and magnetic properties of HEA-Fb [17,21]. Furthermore, micropillar compression tests were conducted by Soler et al., which gave the first insights into its mechanical behavior [24].

This work reports on the mechanical behavior of equiatomic rare earth alloys with an analysis of a consistent set of tensile tests at room temperature (RT) in conjunction with the respective microstructures. Tensile tests are an essential tool for understanding deformation mechanisms [25,26]. This work allows the assessment of the Gibbs paradox regarding the increase of ΔS_{conf}; see chapter 2.1. Pure elements, equiatomic low entropy alloys (LEA) with two elements, equiatomic medium entropy alloys (MEA) with three or four elements, and equiatomic HEA-Fb with five elements are assessed to vary ΔS_{conf}.

2. Configurational Entropy and Solid solution Strengthening

2.1. Configurational Entropy of a Solid solution

The Gibbs free energy is a thermodynamic measure for the stability of phases. In equilibrium, the phase that leads to the minimal Gibbs free energy will form. Gibbs free energy change due to mixture depends on the enthalpy change ΔH_{mix}, temperature T, and mixing entropy change ΔS_{mix} of the system, see eq. (1) [7].

$$\Delta G_{mix} = \Delta H_{mix} - T\Delta \cdot S_{mix} \quad (1)$$

The mixing entropy change ΔS_{mix} is the sum of individual entropy contributions ΔS_i [26]. The change of the mixing entropy ΔS_{mix} in a solid solution is dominated by configurational entropy ΔS_{conf} during mixing (see eq. 2) [15,26].

$$\Delta S_{mix} = \sum \Delta S_i \approx \Delta S_{conf} \quad (2)$$

In an equiatomic multi-element alloy, the share of ΔS_{conf} on the Gibbs free energy is substantial at RT. ΔS_{conf} is suggested to overcome the formation enthalpy of compounds and stabilize the solid solution [7,8,12]. This stabilization of a solid solution follows the maximum entropy production principle [27]. Boltzmann's equation for the ΔS_{conf} change in an ideal solid solution can be calculated as given in eq. (3) [2,5,20,28], with R, the gas constant (8.314 $Jmol^{-1}K^{-1}$) and c_i, the concentration of the i-th component.

$$\Delta S_{conf} = -R \sum_{i=1}^{k} c_i \cdot ln(c_i) \quad (3)$$

A minimal difference is enough to distinguish particles and thus to increase ΔS_{conf}, which is a statistical value only. This increase of ΔS_{conf} is independent of whether these differences are detectable by other techniques (e.g., tensile tests in case of elements with no difference in solid solution strengthening). The Gibbs paradox states that the calculated increase of ΔS_{conf} does not change, regardless of how similar the elements are. Maximum ΔS_{conf} in a solid solution is achieved by equiatomic composition [29]. E.g., for an equiatomic five-element alloy, the increase per mole is $\Delta S_{conf} \approx 1.61 \cdot R$ [5].

2.2. Solid Solution Strengthening

The mechanical properties of an alloy depend on a range of mechanisms that hinder the movement of dislocations and thus increase the external load needed to deform the material. The other mechanisms must be small enough to be negligible to assess the influence that ΔS_{conf} has on the tensile properties of an alloy.

Solid solution strengthening (SSS) increases the tensile strength of alloys. Incorporating foreign atoms in the crystal lattice of the main element distorts the lattice and increases the critical shear stress. The stress fields generated interact with dislocations, hindering or decelerating dislocation motions during plastic deformation [30,31]. The strengthening effect of SSS depends on the differences between the elements involved, e.g., mutual solubility, atomic radii, and valence electron configuration (VEC) [32,33]. On the contrary, the chemical properties of the elements are not considered in the calculation of ΔS_{conf}. This fact leads to the Gibbs paradox since, in practice, the chemical properties of the elements are highly relevant for alloying [34-36].

Strongly differing properties of the elements lead to a significant strengthening of the alloy (SSS > 0). In the case of non-distinguishable atoms, as in pure elements, the solid solution strengthening is zero (SSS = 0). On the one hand, if the alloying elements are very similar but distinguishable, as in the case of the rare earth alloy system Ho-Dy-Y-Gd-Tb (HEA-Fb), the statistical value ΔS_{conf} is high. On the other hand, this alloy system features minimized SSS due to their similar atomic radii. Therefore, HEA-Fb represents a borderline case to the Gibbs paradox. Therefore, this rare-earth-based system offers the possibility to evaluate the isolated effect of high configurational entropy on material strengthening.

2.3. Unintended Microstructural Contributions to Alloy Strengthening

Apart from the solid solution strengthening (SSS), the microstructure plays a crucial role in mechanical properties and material deformation. The isolated influence of the ΔS_{conf} can only be measured if no other mechanisms significantly influence the tensile strength. Therefore, the microstructure of all specimens must be comparable.

According to the Hall-Petch relationship, grain boundaries will increase the strength of alloys [37-39]. The influence of the grain size on the resistance to plastic deformation follows eq. (4) [37,38,40], with yield stress increase due to grain refinement $\Delta\sigma_{HP}$, Hall-Petch parameter k and average grain size d_{Grain}.

$$\Delta\sigma_{HP} = \frac{k}{\sqrt{d_{Grain}}} \quad (4)$$

The applicability of the Hall-Petch relationship to polycrystalline hexagonal close packed (hcp) materials at RT was confirmed by Ono et al. for magnesium [41]. The material parameter k characterizes the strengthening due to grain size effects.

Apart from grain boundaries, the formation of secondary phases can drastically alter the tensile behavior of an alloy. Apart from that, the formation of additional phases drastically reduces the ΔS_{conf} of the alloy. To evaluate the influence of ΔS_{conf} on the tensile properties of an alloy, the formation of secondary phases must be avoided strictly.

3. Materials and Methods

3.1. Compositions of the Investigated Alloys

Table 1 displays the compositions of the alloys used in this work. Single element alloys, equiatomic low (LEA), and medium entropy (MEA) alloys were derived from HEA-Fb Ho-Dy-Y-Gd-Tb, to vary ΔS_{conf}. All alloys have a hexagonal Mg-type structure [18,20], with a purity of the pure elements greater than 99.9%. Given that all tested alloys are single phase, the calculated configurational entropy ranges from $\Delta S_{conf} \approx 0$ for pure elements to $\Delta S_{conf} = 1.61 \cdot R$ for HEA-Fb. The high configurational entropy of $\Delta S_{conf} = 1.61 \cdot R$ for HEA-Fb leads to 17 kJ·mol^{-1} reduction in Gibbs free energy at 1,000°C and 20 kJ·mol^{-}1 at 1,200°C.

Table 1: Compositions used in this work. Pure elements with purity greater than 99.9%. Two to five component system all in equiatomic ratio with ± 1 at. % accuracy

	Number *n* of elements	**ΔS_{conf} in R**	**Composition (equiatomic)**	**Denomination**
pure elements	1	0	Gadolinium (Gd)	Gd
			Terbium (Tb)	Tb
			Dysprosium (Dy)	Dy
			Holmium (Ho)	Ho
			Yttrium (Y)	Y
LEA	2	0.69	Ho-Y	2+Y
			Ho-Dy	2-Y
MEA	3	1.10	Ho-Y-Gd	3+Y
			Ho-Dy-Tb	3-Y
	4	1.39	Ho-Y-Gd-Tb	4+Y
			Ho-Dy-Gd-Tb	4-Y
HEA	5	1.61	Ho-Dy-Y-Gd-Tb	HEA-Fb

In Table 2, the relevant properties of the pure elements are summarized. All pure constituent elements have an hcp lattice structure. It can be assumed that all equiatomic alloys derived from these pure elements must have an hcp lattice structure. The similarity of the pure elements was assessed concerning melting temperature T_M, density ρ at RT, and atomic radii (covalent $r_{covalent}$ and ionic r_{ionic}) given in the literature [23,42-44]. As Gd, Tb, Dy, and Ho are neighbors in der periodic table of elements, their atomic masses show little relative differences. Due to the lanthanide contraction caused by the poor shielding of the 4f electrons, their atomic and trivalent ionic radii decrease with increasing atomic numbers. They are particularly similar, e.g., $\Delta r_{covalent,max} < 3.2\%$ [18]. Y differs the most from the other elements. Consequently, for each MEA and LEA, an alloy composition with very similar elements (without Y; abbr. "-Y") was compared to an alloy with the most different (all containing Y, abbr. "+Y") elements out of this set.

Table 2: Properties of pure elements [23,42-44]

Element	Melting temperature T_M in °C	Density ρ in g·cm^{-3} (at 20°C)	Atomic radius (covalent) $r_{covalent}$ in pm	Atomic radius (ionic) r_{ionic} in pm	Lattice parameter ratio c/a
Gd	1,313	7.9	196	94	1.5904
Tb	1,356	8.3	194	92	1.5811
Dy	1,407	8.6	192	91	1.5735
Ho	1,474	8.8	192	90	1.5698
Y	1,522	4.5	190	93	1.5711

3.2. Arc Melting

During arc melting, some elements tend to evaporate more than others. This evaporation changes the chemical compositions of the specimens in the as-cast state compared to the weighed initial equimolar compositions. Figure 2 b) shows a melted specimen, for example. All as-cast chemical compositions were evaluated via micro-X-Ray Fluorescence analyzer (µ-XRF) Orbis PC by Ametek at 45 kV and 700 µA. Before measurement, the surface oxidation layers on the specimens were removed by grinding with SiC paper (Grid 600). Three areas with a 1 mm diameter were measured on each knob-shaped specimen to detect deviations from the equiatomic target compositions. The chemical compositions were adjusted via linear interpolation to optimize the equiatomic composition for HEA-Fb ± 0.5 at.%. This careful adjustment of the ingots was applied to all tested alloys, leading to increased accuracy of equiatomic compositions to less than ± 1.6 at.%. This accuracy ensures that the deviations of ΔS_{conf} concerning the ideal equiatomic ΔS_{conf} are less than 0.07%.

Figure 1 a) shows the geometry of an arc melted knob of a HEA-Fb specimen. All specimens weigh about 30 g and are made from element granules. The specimens were prepared with an arc melter AM 500 by Bühler in an argon atmosphere at 520 mbar after three evacuation steps. Ti was used as an oxygen getter before melting the alloys. Arc melting ensures the complete melting of all alloying components. All specimens were melted three times to homogenize with a W electrode on a water-cooled copper crucible plate [5,16].

3.3. Specimen Preparation

Figure 1 b) shows a metallographically prepared cross-section of the knob-shaped specimen for the microstructure analysis. A specimen piece of each alloy was separated via the precision cut-off machine BRILLIANT 240 and mounted in PolyFast with a hot mounting press Opal X-Press by ATM. As rare earth metals are susceptible to oxidation [12], limiting oxidation and corrosion was challenging throughout preparation and testing. The specimens were ground by hand with Silicon

carbide (SiC) grinding paper on a wet grinding machine LaboPol-21 by Struers up to Grit 2.500. After 1,000 SiC grinding, the specimens were ground with ethanol instead of water. Next, the specimens were automatically polished with the polishing machine SAPHIR 560 by ATM with 20 N, at 200 rpm, for five minutes each with 3 µm and 1 µm water-free diamond suspension on MD-DAC discs. As the last step, the specimens were polished with water-free oxide polish (OP) for five minutes. The specimens were cleaned in an ultrasonic ethanol bath and handled with great care between each preparation step. The microanalysis and mechanical testing were conducted shortly after preparation to minimize oxidation of the surfaces of the cross sections. The specimens were carefully stored in a vacuum desiccator at a pressure of approximately 100 mbar.

Figure 1 c) shows the geometry of the miniature tensile specimens. These tensile specimens were cut from the knob-shaped specimens using the wire-cutting EDM machine CUT 200 SP by Agiecharmilles. The tensile specimens have a gauge length of 5 mm, and a cross-sectional area of 0.9 mm x 0.9 mm. Immediately before placing the tensile specimens in the specimen holder of the tensile test rig, the surface oxidation layer on the specimens was removed by grinding with SiC paper (Grid 600) as far as possible.

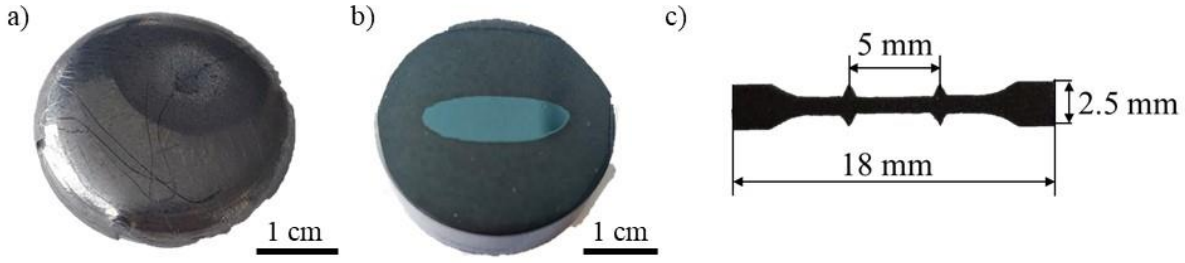

Figure 1: a) as-cast knob-shaped HEA-Fb specimen; b) cross-section of as-cast specimen; c) tensile specimen geometry

3.4. Grain Size Measurement

Grain refinement leads to increased tensile strength and might therefore obscure an entropy effect's strengthening of the alloy. To assess the magnitude of the grain boundary strengthening via the Hall-Petch relation in eq. (4) the grain structure was analyzed via an optical microscope (OM) using polarized light. The average grain sizes d_{Grain} were averaged from 25 randomly chosen grains in an OM image using the software ImageJ. For HEA-Fb, no value for the stress concentration factor k is available in the literature. As HEA-Fb has a magnesium-type hcp structure, k values for magnesium are used as a rough estimate to calculate a possible strength effect due to grain size in HEA-Fb and all other tested materials.

3.5. Phase Analysis

Secondary phases strongly influence the tensile behavior of the alloys and thus disguise a possible strengthening effect of ΔS_{conf}. The phase analysis of HEA-Fb was carried out with an X-Ray diffractometer (XRD) D8 Advance (Brucker). The XRD measurement was performed between diffraction angles 2Θ of 20-90° with a step width of 0.02° and a time of 0.5 s per measurement step.

The measured XRD pattern was compared with the International Center for Diffraction Data powder diffraction file (ICCD-PDF) PDF-4+ 2021 database to identify possible phases in the specimen.

While the XRD result of HEA-Fb gives the average chemical composition and information on phases present in the entire measurement region on the specimen, energy-dispersive X-Ray spectroscopy (EDS) provides spatially resolved elemental distribution information. To find local inhomogeneities, scanning electron microscopy (SEM) 1540EsB Cross Beam (Zeiss) with a secondary electron (SE) detector was performed on specimens together with corresponding elemental mappings via energy-dispersive X-Ray spectroscopy Thermo Noran System Six (EDS). For the elemental mappings, an acceleration voltage of 20 kV at a working distance of 8 mm was applied with a minimal test time of 60 minutes.

3.6. Tensile Testing

Tensile tests were carried out at a 0.01 $mm \cdot min^{-1}$ truss velocity with the universal testing machine Z 2.5/T13S (Zwick) at RT. This deformation speed corresponds to a technical strain rate of about $\dot{\varepsilon} \approx 10^{-3}\ s^{-1}$. The elongation measurement was carried out with a video extensometer; for a detailed description, see [45]. At least two valid tensile tests per alloy were conducted to account for the possible scatter of the measured values. The tests enable the evaluation of possible strengthening effects through ΔS_{conf} itself.

4. Results

4.1. Grain Sizes of the As-Cast Specimens

Figure 2 shows optical microscope (OM) images of the microstructures of all specimens compared in the as-cast state. The grain structures are visible in all images. The alloys include twin grain boundaries in the as-cast state, marked on the Tb specimen.

Figure 2 compares the average grain diameters d_{Grain} of all specimens. Tb shows the most prominent grains compared to all tested specimens, with the largest average grain diameter of 1.139 µm. In the bottom right corner of Figure 2, HEA-Fb shows a medium average grain diameter of 521 µm. The average values of grain diameters range from 350 µm to about 1,200 µm. In the center of the knob specimens, elongated columnar grains have formed.

In contrast, the Ho specimen shows more round grains without a preferential orientation. In the arc melter, the high cooling rates near the water-cooled copper crucible plate cause rounder grain shapes, while slower cooling rates in the center of the knob-shaped specimens will result in more elongated grain shapes. Additionally, on some specimens, e.g., pure elements and MEA 3+Y displayed in Figure 2, black oxide particles are visible as substructures all over the cross-section. Small volume fractions of oxides inside the alloys will not influence the mechanical properties significantly [46], and the surfaces of the specimens have been ground with 800 SiC paper before tensile testing.

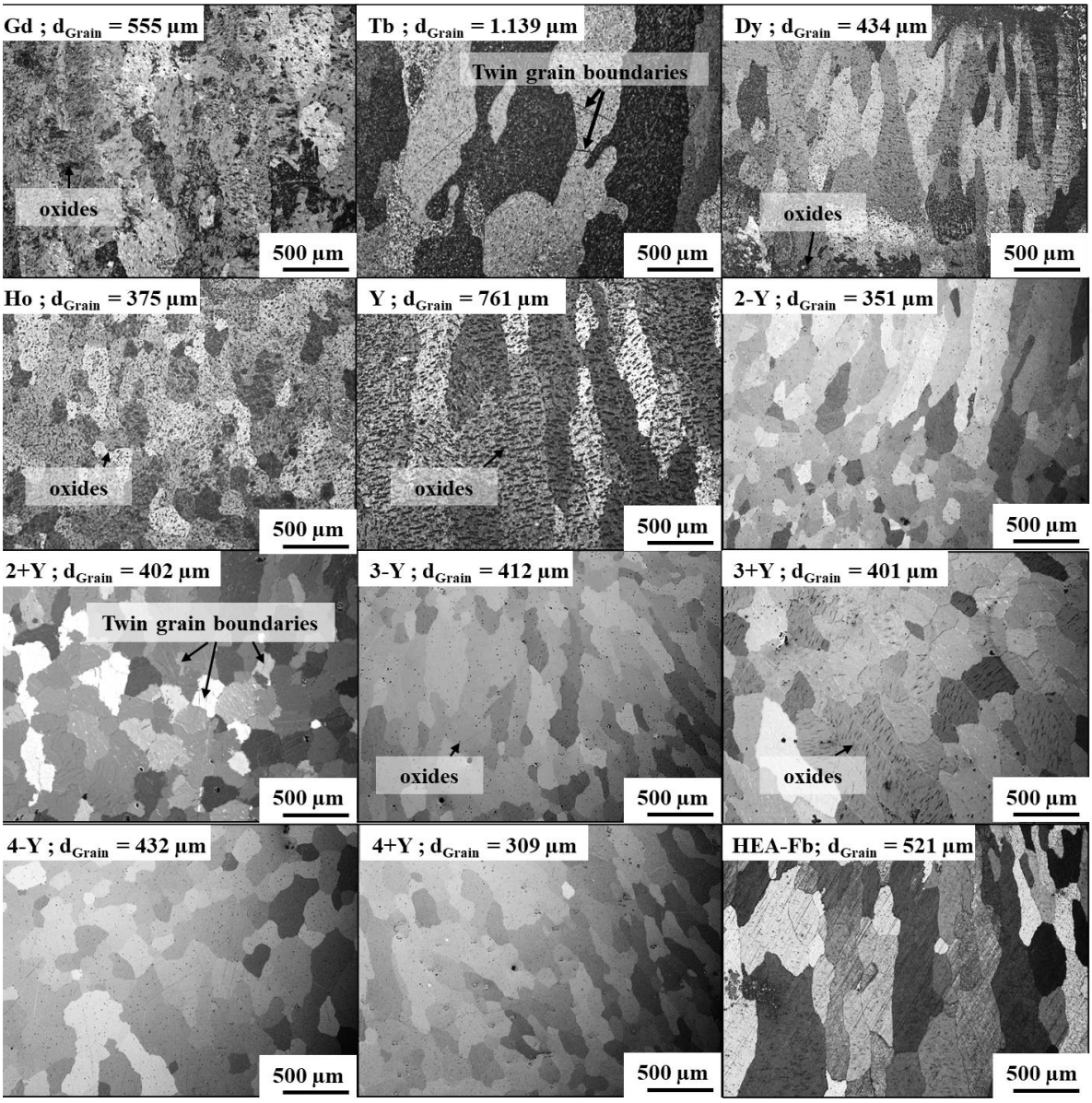

Figure 2: OM images with polarized light of the as-cast microstructures of all specimens (see Table 1) and the average of grain diameter

4.2. XRD Analysis of HEA-Fb

Figure 3 plots the relative intensity of the X-Ray diffraction (XRD) pattern from HEA-Fb over the diffraction angle 2Θ. This XRD measurement confirms HEA-Fb as a hexagonal and single-phase alloy. From the PDF-4+ 2021 database, the HEA-Fb is characterized by the following near-equiatomic composition: $Y_{0.205}$-$Gd_{0.211}$-$Tb_{0.196}$-$Dy_{0.195}$-$Ho_{0.193}$ (PDF 04-022-6351) with a lattice parameter ratio of c/a 1.597 [20]. Jelen et al. found cubic Dy precipitates (PDF 04-003-4708) in HEA-Fb specimens produced by high-frequency levitation casting [21]. The obtained XRD pattern was compared to the XRD pattern from the cubic precipitates found by Jelen et al. [21], and no cubic or other precipitates were found [21]. The tested HEA-Fb alloy can be considered single-phase, as there was no evidence for secondary phases or precipitates.

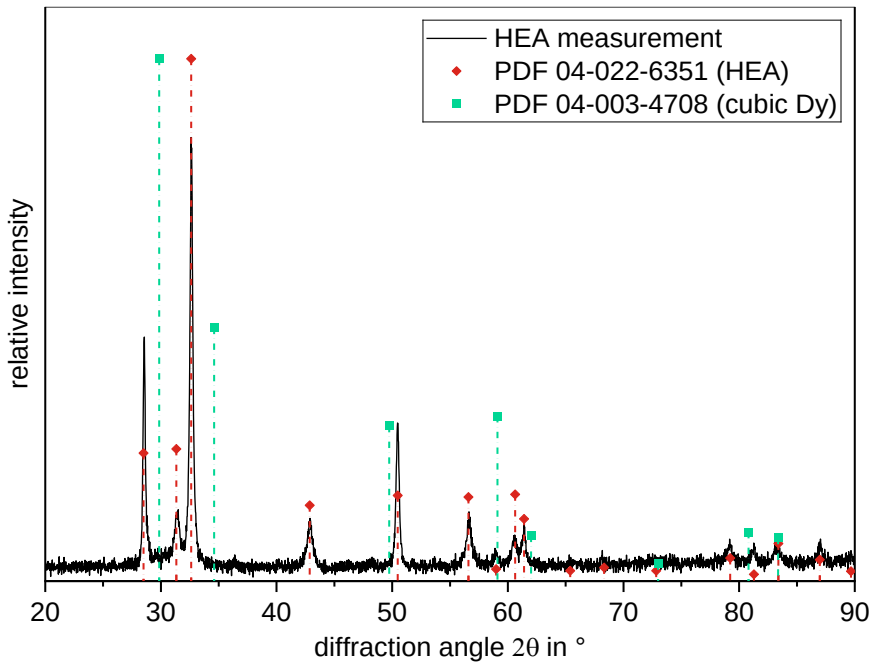

Figure 3: XRD pattern of investigated HEA-Fb

4.3. EDS Mappings of As-Cast specimens

Figure 4 a) shows an SEM (SE2) image of the MEA 3-Y along with the corresponding EDS elemental mappings of the constituent elements and the oxygen content in at. % in Figure 4 b) - d). The results depict a homogeneous elemental distribution of Tb, Dy, and Ho with 33 ± 5 at.%.

Slightly increased oxidation was measured at the grain boundaries, see labeling in Figure 4 a). No secondary phases are found in this MEA. This result is representative of all tested alloys without Y. 2-Y, 3-Y, and 4-Y contain the most similar elements of the alloy system, see Table 2.

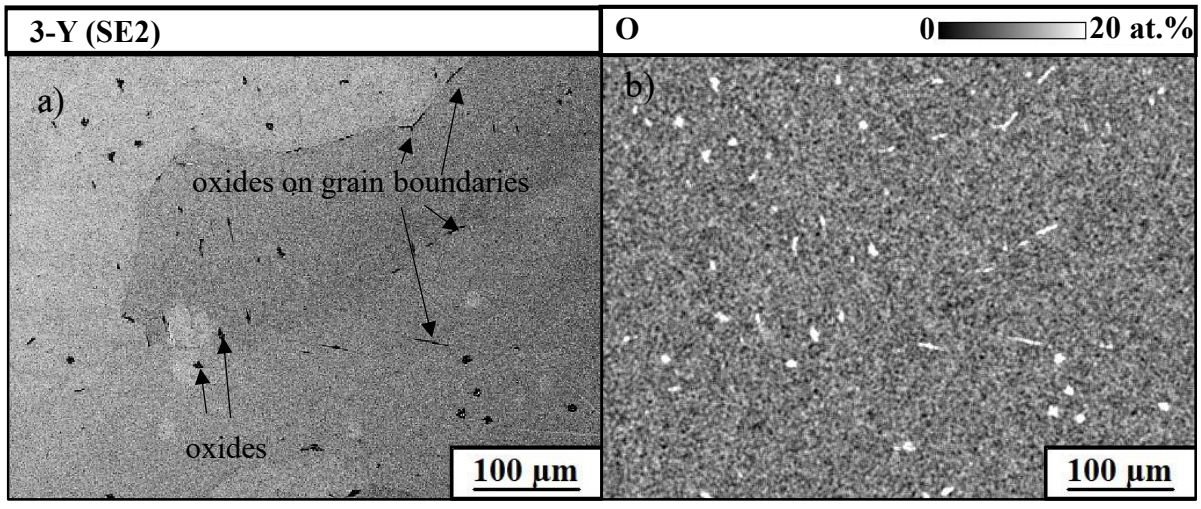

Figure 4: SEM (SE2) image of 3-Y alloy and elemental mapping (EDS) of oxygen (O) in at.%. Homogeneous distribution of elements (not shown here)

Figure 5 a) shows a SEM (SE2) image of the LEA 2+Y and Figure 5 c) shows the MEA 3+Y and their corresponding elemental mappings of Y in Figure 5 b) and d) in at.%. Other than in 3-Y, these alloys contain yttrium-rich secondary phases, preferably along the grain boundaries. A slight depletion of Y

was measured inside the grain, e.g., in 2+Y the Y content is about 44 ± 5 at.%. In 3+Y, the other two elements are homogeneously distributed (not shown here).

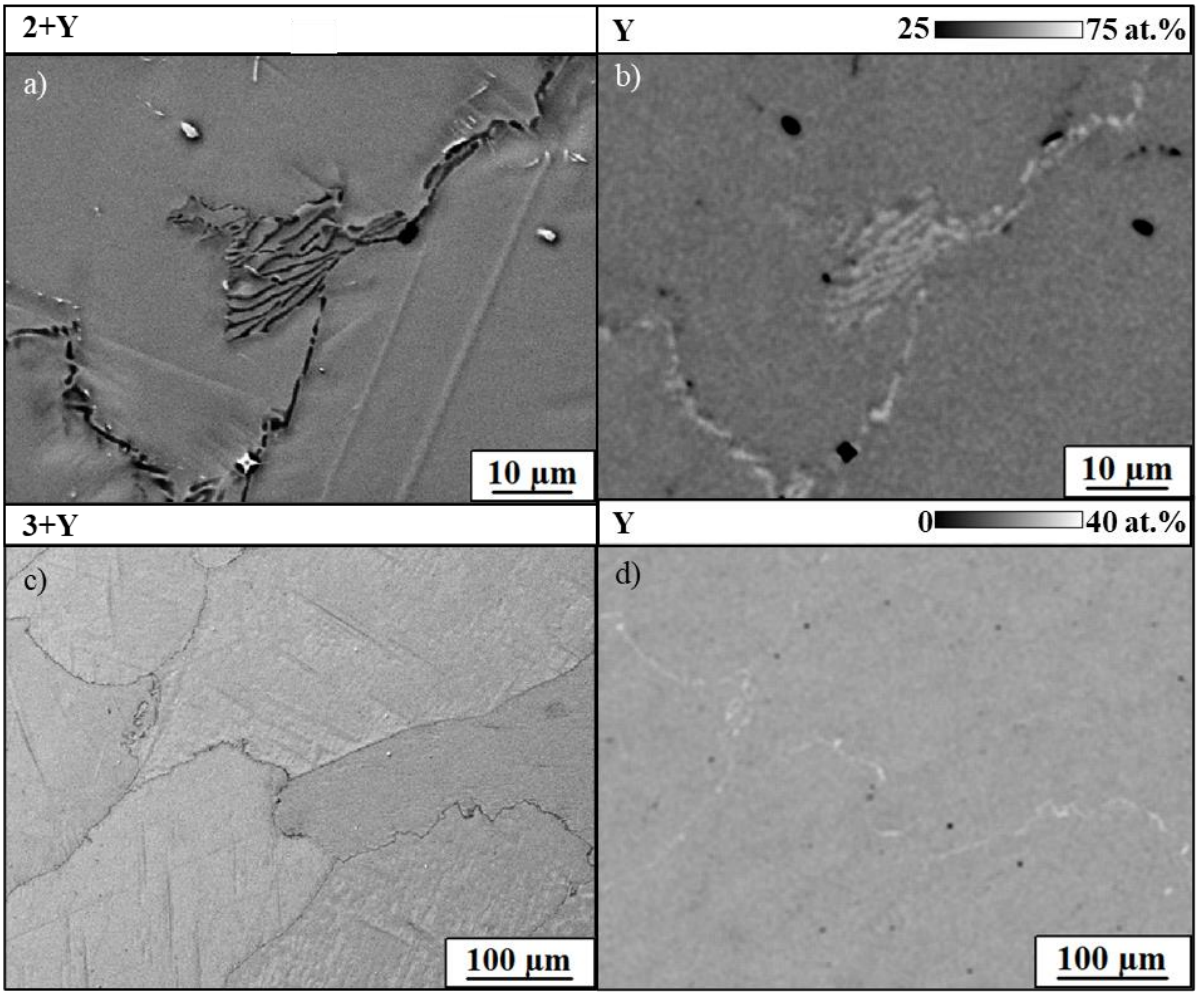

Figure 5: SEM (SE2) image of a) 2+Y and c) 3+Y alloy and their respective elemental mapping (EDS) of the constituent element Y in at. %

Figure 6 shows no Y-rich secondary phase for HEA-Fb, as expected from the XRD measurement. In line with the other alloys, HEA-Fb contains increased oxides at the grain boundaries. Along with oxides from inner oxidation, additional oxides at the surface of the specimen, preferably along grooves from the grinding process, are visible. Apart from these oxides (around 10 at. %), the chemical composition inside the grains is relatively homogeneous (17 ± 4 at.%). Overall, a homogeneous single-phase HEA has been produced. A single-phase state is necessary to evaluate the influence of ΔS_{conf} on its tensile behavior.

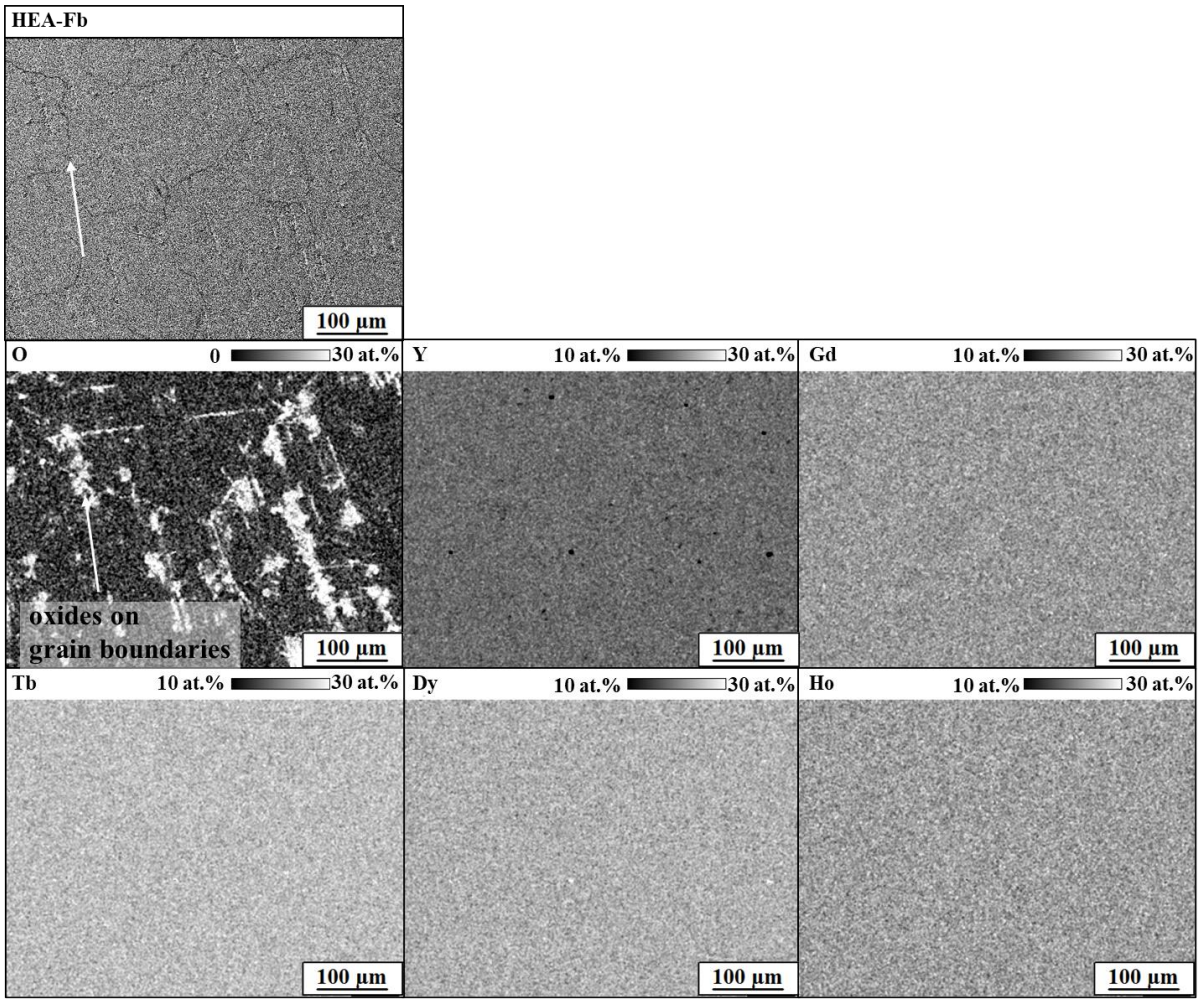

Figure 6: SEM (SE2) image of HEA-Fb alloy and elemental mappings (EDS) of the constituent elements Y, Tb, Dy, Ho as well as oxygen (O) in at. %

4.4. Tensile Behavior

In Figure 7, representative RT stress-strain curves for all considered alloys are displayed. To assess the characteristic tensile properties, ultimate tensile strength (UTS), yield strength (YS), and strain to failure (ε_f), at least two valid tensile tests were performed and averaged for each alloy. The average UTS of all alloys is between 108 MPa for Gd to 240 MPa for Dy. At the same time, YS ranges from 78 MPa for 4+Y to 171 MPa for Dy. Dy exhibits the highest tensile strength of all tested specimens. The tensile strength of HEA-Fb is in the middle range of all tested alloys. In Table 3, the tensile properties of all tested alloys are summarized together with the standard deviation.

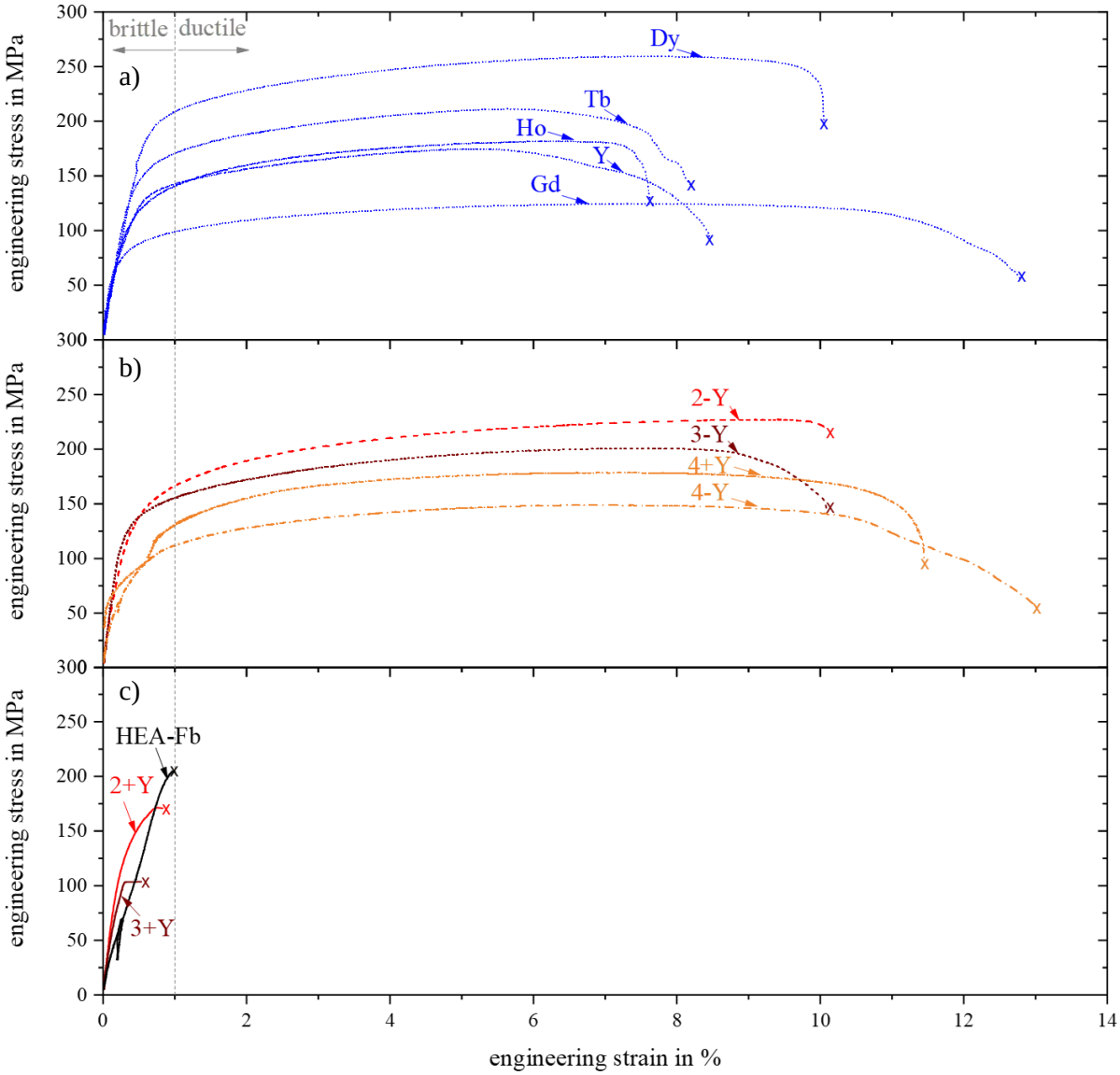

Figure 7: Stress-Strain curves from tensile testing of all alloys given in Table 1. Pure elements in a), ductile alloys in b) and brittle alloys in c)

All pure elements are shown in Figure 7 a), the ductile alloys are shown in Figure 7 b), and all brittle alloys are shown in Figure 7 c). Most tested alloys exhibit comparable ductility except for 2+Y, 3+Y, and HEA-Fb, which show a pronounced brittle behavior. These brittle alloys in Figure 7 c) contain Y and have a strain to failure of only up to 1%. All pure elements in Figure 7 a), as well as the alloys that do not contain Y plus the MEA 4+Y in Figure 7 b), are more ductile with ε_f of 8 to 12%. In Table 3, along with the results of tensile tests, secondary phases detected via EDS, as well as visible twin grain boundary formation in the as-cast state are summarized for all tested alloys.

Table 3: Average values of UTS, YS and strain to failure from tensile tests with standard deviations as well as detection of secondary phases or twins in the as-cast state in all tested alloys.

Alloy type	*UTS* in MPa	*YS* in MPa	ε_f in %	Other phases detected	Twins in as-cast state
Gd	108 ± 16	83 ± 3	11.2 ± 1.2	No	Yes
Tb	196 ± 8	142 ± 2	9.3 ± 1.2	No	Yes
Dy	240 ± 17	171 ± 10	9.8 ± 0.9	No	Yes
Ho	187 ± 6	128 ± 1	7.9 ± 0.5	No	Yes
Y	180 ± 3	100 ± 3	8.4 ± 0.3	No	No
2+Y	165 ± 7	151 ± 1	0.7 ± 0.2	Yes	Yes
2-Y	230 ± 1	123 ± 20	10.8 ± 0.7	No	Yes
3+Y	113 ± 10	111 ± 8	0.5 ± 0.0	Yes	Yes
3-Y	197 ± 2	132 ± 1	10.1 ± 1.3	No	Yes
4+Y	169 ± 10	78 ± 1	12.8 ± 1.4	No	Yes
4-Y	137 ± 11	85 ± 4	12.3 ± 0.8	No	Yes
HEA-Fb	204 ± 1	165 ± 27	1.0 ± 0.1	No	Yes

5. Discussion

5.1. Microstructural Influence on Tensile Behavior

The possible influence of the grain size on the plastic deformation behavior during the mechanical characterization depends on the Hall-Petch parameter *k*, which is unknown for HEA-Fb and all other tested alloys [47]. As a broad approximation, the factor *k* for magnesium is assumed for the tested alloys, with literature values ranging from $k = 150$ MPa·µm$^{1/2}$ to $k = 294$ MPa·µm$^{1/2}$ [39,47-50]. Along with the measured grain diameters d_{Grain} of all alloys between 350 µm to 1,200 µm, the calculated difference in tensile strength following eq. (4) is in the range of $\Delta\sigma_{HP} = 4.3$ MPa to 15.7 MPa. The estimated Hall-Petch influence has the same magnitude as the obtained tensile test scatter. As such, the influence of different grain sizes on our specimens' tensile behavior is negligible.

In Table 3, detected secondary phases, as well as twin grain boundaries, are summarized. The most brittle specimens, with strain to failure under 1%, are 2+Y, 3+Y, and HEA-Fb. The Y-containing alloys 2+Y and 3+Y were both found to contain secondary phases. This multiphase state explains the observed brittle behavior of the alloys compared to the other alloys of this study. The Y-containing alloy 4+Y shows significantly more ductile behavior, indicating that this alloy contains no secondary phases that lead to embrittlement.

Although the brittle HEA-Fb does not show any secondary phases either in XRD or EDS, its pronounced brittle behavior indicates previously undiscovered additional phases. Very small secondary precipitates are not measurable with XRD or EDS, as discussed elsewhere [3,51,52]. Soler

et al. recently showed the formation of secondary phases in HEA-Fb, which produced HEA-Fb via high-frequency levitation cast melting. XRD measurements revealed that the HEA-Fb specimens included lens-shaped cubic Dy precipitates [24].

All specimens except pure Y contain visible twin grain boundaries in their as-cast states, see Table 3. This result underlines the differences between Y and all other tested alloys. Concerning all alloys and pure elements, we find no sign of significant differences in the underlying plastic deformation mechanisms.

5.2. Strengthening Effect of Configurational Entropy on Tensile Behavior

Figure 8 shows the tensile properties UTS, YS, and strain to failure ε_f at RT plotted versus ΔS_{conf}. The alloys 2+Yand 3+Y are not included in this data as they were found not to form single-phase alloys. ΔS_{conf} ranges from zero for the pure elements to 1.61·R or 13.4 J·mol^{-1}K^{-1} for HEA-Fb. The range in which the tensile properties vary, including maximum deviations, is indicated by grey shading.

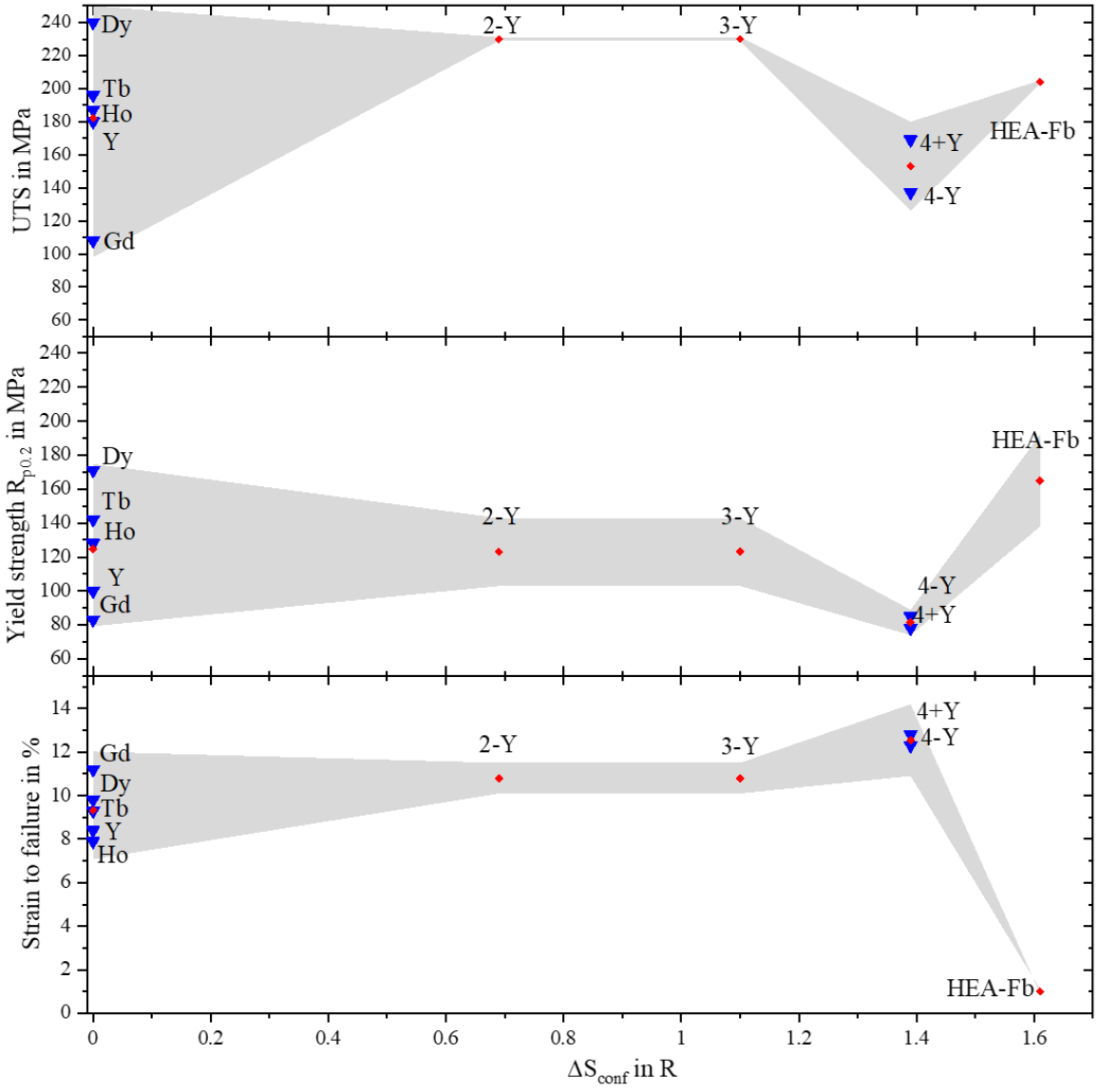

Figure 8: Average tensile behavior a) UTS, b) YS and c) strain to failure ε_f with maximum deviations over configurational entropy ΔS_{conf} for all tested alloys at RT

From Figure 8, no significant trends in the tensile test data at RT can be obtained. The UTS (Figure 8 a)) of 2-Y, 3-Y, and HEA-Fb lie in the range of the UTS of the pure elements. These results prove the minimized SSS of this alloy system. For the MEA 4+Y and 4-Y, the UTS slightly decrease, but they are still in the range of the UTS of the pure elements. The YS (Figure 8 b)) follows the same trends as the UTS, and no direct correlation to ΔS_{conf} was measured. While the YS is slightly decreased for the four-element MEA 4+Y and 4-Y, it is slightly increased for the HEA-Fb. As Dy shows the highest YS of all alloys, no high entropy effect on strength was found. The strain to failure ε_f (Figure 8 c)) does not increase from pure elements to 3-Y MEA; it is slightly increased for 4+Y and 4-Y. This trend is not shown by HEA-Fb, as this alloy's strain to failure sharply decreases. This substantial reduction of strain to failure ε_f identifies HEA-Fb as an outlier. The brittleness of this alloy indicates other phases in the alloy that have not yet been discovered. Another possible explanation for this brittle fracture behavior is the influence of oxides in the HEA-Fb specimens, which cannot be avoided despite careful specimen handling. Gali and George stated that tiny volume fractions of oxides in specimens would not significantly influence the mechanical properties [46].

Furthermore, oxides also appeared inside the other alloys and did not cause embrittlement here. Consequently, the oxides will not be crucial for the brittleness of HEA-Fb, but undiscovered secondary phases are likely to cause the observed embrittlement. Continued phase analysis will be subject to future TEM investigations of the HEA-Fb alloy system.

There is no correlation between increasing ΔS_{conf} and increasing strength or ductility for the tested hexagonal rare earth high entropy alloy Ho-Dy-Y-Gd-Tb (HEA-Fb) at RT considering all tensile test results. ΔS_{conf} is not the controlling variable for the tensile behavior of the specimens; other factors determine the performance of the alloys.

The Ho-Dy-Y-Gd-Tb (HEA-Fb) alloy system provides an excellent case to investigate the Gibbs paradox for HEA, because of their highly similar chemical properties. In contrast, when considering the statistical value ΔS_{conf} from eq. (3), only the concentrations of elements are considered. From the tensile test results with a systematic variation of ΔS_{conf}, it is evident that it is an unallowable simplification to derive the mechanical behavior from ΔS_{conf} alone.

The obtained data indicate that the effect of a high ΔS_{conf} provides a lower proportion of total strength at RT, which challenges the assumption of a high entropy effect. This conclusion is in line with other works, and the validity of a high entropy effect on the SSS of HEA is increasingly discussed [8,52,53]. For example, Zhao et al. found no strengthening effect of the rare-earth-based HEA Gd-Ho-La-Tb-Y, where the mechanical properties obey the Rule of Mixture [54]. Also, for the well-researched Cantor alloy, which has proven advantageous properties at low temperatures, the creep strength showed no influence of ΔS_{conf} alone [55]. As Manzoni and Glatzel resume, no new strengthening mechanisms unique to HEA have been found so far [56]. In line with that, we conclude that other effects than ΔS_{conf} govern the tensile strength of hexagonal rare earth HEA-Fb at RT.

6. Conclusions

To the best of our knowledge, the presented results contain the first consistent set of tensile properties of the hexagonal rare earth high entropy alloy system Ho, Dy, Y, Gd, and Tb together with low, medium, and high entropy alloys at RT. The pure elements show remarkably similar properties, which provides a suitable model system to explore the tensile behavior of high entropy alloys with minimized solid solution strengthening. A variation of configurational entropy ΔS_{conf} was accomplished by performing tensile tests at room temperature (RT) with equiatomic alloys of up to five elements. The following conclusions can be drawn:

1. Most tested alloys, including the high entropy alloy Ho-Dy-Y-Gd-Tb, exhibit a single-phase homogeneous elemental distribution in the as-cast state. The alloys Ho-Y and Ho-Y-Gd form Y-rich secondary phases at the grain boundaries. All specimens produced by arc melting show homogeneous microstructures in the as-cast state with grain sizes of about 350 - 1200 µm.
2. All tested low, medium, and high entropy alloys show ultimate tensile strengths and yield strengths in the range of the tested pure elements. The alloys with observed secondary phases, Ho-Y and Ho-Y-Gd, and the high entropy alloy behave brittle during tensile testing with strain to failures less than 1%.
3. For the alloy system Ho-Dy-Y-Gd-Tb, there is no direct correlation between the ΔS_{conf} and the tensile properties ultimate tensile strength, yield strength, and strain to failure at RT. As evident in Figure 8, the low, medium, and high entropy alloys show no tensile strengthening resulting from their increased ΔS_{conf}.
4. Ho-Dy-Y-Gd-Tb has proven to be a model system with minimized solid solution strengthening. It is a suitable alloy system for investigating fundamental concepts in material science, e.g., the Gibbs paradox.

Acknowledgments

The authors are grateful to the German Research Foundation (DFG) for the financial support by GL181/56–2 and FE 571/4-2, and through the Priority Program SPP 2006 “Compositionally Complex Alloys – High Entropy Alloys (CCA-HEA)”.

References

[1] Cantor B., Chang I., Knight P., Vincent A.; *Microstructural development in equiatomic multicomponent alloys*; Materials Science and Engineering: A 375-377, (2004), 213-218. doi:10.1016/j.msea.2003.10.257

[2] Yeh J.-W., Chen S.-K., Lin S.-J., Gan J.-Y., Chin T.-S., Shun T.-T., Tsau C.-H., Chang S.-Y.; *Nanostructured High-Entropy Alloys with Multiple Principal Elements: Novel Alloy Design Concepts and Outcomes*; Advanced Engineering Materials 6, (2004), 299-303. doi:10.1002/adem.200300567

[3] George E.P., Raabe D., Ritchie R.O.; *High-entropy alloys*; Nature Reviews Materials 4, (2019), 515-534. doi:10.1038/s41578-019-0121-4

[4] *Gao, M.C.; Yeh, J.-W.; Liaw, P.K. et al. (eds.); High-Entropy Alloys – Fundamentals and applications.* Springer International Publishing, Cham, 2016.

[5] Murty, B.S.; Yeh, J.-W.; Ranganathan, S.; *High-entropy alloys.* BH Butterworth-Heinemann an imprint of Elsevier, Amsterdam, 2014.

[6] Kozak R., Sologubenko A., Steurer W.; *Single-phase high-entropy alloys – an overview*; Zeitschrift für Kristallographie - Crystalline Materials 230, (2015), 55-68. doi:10.1515/zkri-2014-1739

[7] Zhang Y., Zuo T.T., Tang Z., Gao M.C., Dahmen K.A., Liaw P.K., Lu Z.P.; *Microstructures and properties of high-entropy alloys*; Progress in Materials Science 61, (2014), 1-93. doi:10.1016/j.pmatsci.2013.10.001

[8] Nutor R.K., Cao Q., Wang X., Zhang D., Fang Y., Zhang Y., Jiang J.-Z.; *Phase Selection, Lattice Distortions, and Mechanical Properties in High-Entropy Alloys*; Advanced Engineering Materials 22, (2020), 2000466. doi:10.1002/adem.202000466

[9] Ranganathan S.; *Alloyed pleasures: Multimetallic cocktails*; Current science, (2003).

[10] Yeh J.W.; *Recent progress in high-entropy alloys*; Annales de Chimie. Science des Materiaux (Paris) 31, (2006), 633-648.

[11] Yeh J.-W.; *Alloy Design Strategies and Future Trends in High-Entropy Alloys*; JOM 65, (2013), 1759-1771. doi:10.1007/s11837-013-0761-6

[12] Qiao J.W., Bao M.L., Zhao Y.J., Yang H.J., Wu Y.C., Zhang Y., Hawk J.A., Gao M.C.; *Rare-earth high entropy alloys with hexagonal close-packed structure*; Journal of Applied Physics 124, (2018), 195101. doi:10.1063/1.5051514

[13] Li R., Xie L., Wang W.Y., Liaw P.K., Zhang Y.; *High-Throughput Calculations for High-Entropy Alloys: A Brief Review*; Frontiers in Materials 7, (2020). doi:10.3389/fmats.2020.00290

[14] Zhang C., Gao M.C.; *CALPHAD Modeling of High-Entropy Alloys. In: Gao, M.C.; Yeh, J.-W.; Liaw, P.K. et al.* (eds.): High-Entropy Alloys – Fundamentals and applications. Springer International Publishing, Cham, 2016, 399-444.

[15] Gao M.C., Zhang B., Guo S.M., Qiao J.W., Hawk J.A.; *High-Entropy Alloys in Hexagonal Close-Packed Structure*; Metallurgical and Materials Transactions A 47, (2016), 3322-3332. doi:10.1007/s11661-015-3091-1

[16] Li R.-X., Qiao J.-W., Liaw P.K., Zhang Y.; *Preternatural Hexagonal High-Entropy Alloys: A Review*; Acta Metallurgica Sinica (English Letters) 33, (2020), 1033-1045. doi:10.1007/s40195-020-01045-9

[17] Feuerbacher M., Heidelmann M., Thomas C.; *Hexagonal High-entropy Alloys*; Materials Research Letters 3, (2015), 1-6. doi:10.1080/21663831.2014.951493

[18] Voncken, J.; *The Rare Earth Elements – An Introduction*, SpringerBriefs in Earth Sciences, Springer International Publishing, Cham, 2016.

[19] Platt A. W. G.; *Group trends. In: Atwood, D.A.* (ed.): The rare earth elements – Fundamentals and applications, EIC Bks. John Wiley & Sons Inc, Chichester, West Sussex, United Kingdom, 2013.

[20] Lužnik J., Koželj P., Vrtnik S., Jelen A., Jagličić Z., Meden A., Feuerbacher M., Dolinšek J.; *Complex magnetism of Ho-Dy-Y-Gd-Tb hexagonal high-entropy alloy*; Physical Review B 92, (2015). doi:10.1103/PhysRevB.92.224201

[21] Jelen A., Jae Hyuck Jang, Junhyup Oh, Hae Jin Kim, Anton Meden, Stane Vrtnik, Michael Feuerbacher, Janez Dolinšek; *Nanostructure and local polymorphism in "ideal-like" rare-earths-based high-entropy alloys*; Materials Characterization 172, (2021), 110837. doi:10.1016/j.matchar.2020.110837

[22] Vrtnik S., Lužnik J., Koželj P., Jelen A., Luzar J., Krnel M., Jagličić Z., Meden A., Feuerbacher M., Dolinšek J.; *Magnetic phase diagram and magnetoresistance of Gd–Tb–Dy–Ho–Lu hexagonal high-entropy alloy*; Intermetallics 105, (2019), 163-172. doi:10.1016/j.intermet.2018.10.014

[23] Sicius, H.; *Handbuch der chemischen Elemente – [engl. Handbook of the chemical elements]*, Springer Reference, Springer Spektrum, Berlin, (2021).

[24] Soler R., Evirgen A., Yao M., Kirchlechner C., Stein F., Feuerbacher M., Raabe D., Dehm G.; *Microstructural and mechanical characterization of an equiatomic YGdTbDyHo high entropy alloy with hexagonal close-packed structure*; Acta Materialia 156, (2018), 86-96. doi:10.1016/j.actamat.2018.06.010

[25] Manzoni A.M., Haas S., Daoud H., Glatzel U., Förster C., Wanderka N.; *Tensile Behavior and Evolution of the Phases in the Al10Co25Cr8Fe15Ni36Ti6 Compositionally Complex/High Entropy Alloy*; Entropy (Basel, Switzerland) 20 (2018), 646. doi:10.3390/e20090646

[26] Zhang W., Liaw P.K., Zhang Y.; *Science and technology in high-entropy alloys*; Science China Materials 61, (2018), 2-22. doi:10.1007/s40843-017-9195-8

[27] Martyushev L.M., v. d. Seleznev; *Maximum entropy production principle in physics, chemistry and biology*; Physics Reports 426 (2006), 1-45. doi:10.1016/j.physrep.2005.12.001

[28] Stephan P., Schaber K., Stephan K., Mayinger F.; *Thermodynamische Prozesse, Maschinen und Anlagen – [engl. Thermodynamic Processes, Machinery and Equipment].* Stephan, P.; Schaber, K.; Stephan, K. *et al.* (Hrsg.): Thermodynamik // Einstoffsysteme – [engl. Thermodynimics // Single-component systems], Springer-Lehrbuch Vol. 1. Springer Vieweg, Berlin, Heidelberg; Springer Vieweg, Berlin, (2013), 319-397.

[29] Gadelmeier C., Haas S., Lienig T., Manzoni A., Feuerbacher M., Glatzel U.; *Temperature Dependent Solid Solution Strengthening in the High Entropy Alloy CrMnFeCoNi in Single Crystalline State*; Metals 10, (2020), 1412. doi:10.3390/met10111412

[30] Labusch R.; *Statistische theorien der mischkristallhärtung*; Acta Metallurgica 20, (1972), 917-927. doi:10.1016/0001-6160(72)90085-5

[31] Fleischer R.; *Substitutional solution hardening*; Acta Metallurgica 11, (1963), 203-209. doi:10.1016/0001-6160(63)90213-X

[32] Rösler, J.; Harders, H.; Bäker, M.; *Mechanisches Verhalten der Werkstoffe – [engl. Mechanical behavior of the materials].* Springer Fachmedien Wiesbaden, Wiesbaden, (2012).

[33] Gottstein, G.; *Materialwissenschaft und Werkstofftechnik – [engl. Materials science and materials engineering].* Springer Berlin Heidelberg, Berlin, Heidelberg, (2014).

[34] Saunders S.; *The Gibbs Paradox*; Entropy (Basel, Switzerland) 20 (2018), 552. doi:10.3390/e20080552

[35] Gibbs, J.W.; *Elementary principles in statistical mechanics: developed with especial reference to the rational foundations of thermodynamics.* C. Scribner's sons, (1902).

[36] Haas S., Mosbacher M., Senkov O.N., Feuerbacher M., Freudenberger J., Gezgin S., Völkl R., Glatzel U.; *Entropy Determination of Single-Phase High Entropy Alloys with Different Crystal Structures over a Wide Temperature Range*; Entropy (Basel, Switzerland) 20 (2018). doi:10.3390/e20090654

[37] Hall E.O.; *The Deformation and Ageing of Mild Steel: III Discussion of Results*; Proceedings of the Physical Society. Section B 64, (1951), 747-753. doi:10.1088/0370-1301/64/9/303

[38] Petch N.J.; *The Cleavage Strength of Polycrystals*; Journal of the Iron and Steel Institute 174, (1953), 25-28.

[39] Cordero Z.C., Knight B.E., Schuh C.A.; *Six decades of the Hall–Petch effect – a survey of grain-size strengthening studies on pure metals*; International Materials Reviews 61, (2016), 495-512. doi:10.1080/09506608.2016.1191808

[40] Armstrong R.W.; *The influence of polycrystal grain size on several mechanical properties of materials*; Metallurgical and Materials Transactions B 1, (1970), 1169-1176. doi:10.1007/BF02900227

[41] Ono N., Nowak R., Miura S.; *Effect of deformation temperature on Hall–Petch relationship registered for polycrystalline magnesium*; Materials Letters 58, (2004), 39-43. doi:10.1016/S0167-577X(03)00410-5

[42] Scott T.E.; *Chapter 8 Elastic and mechanical properties. In: Gschneidner, K.A.; Eyring, L.; Maple, M.B.* (eds.): Metals, Handbook on the Physics and Chemistry of Rare Earths Vol. 1. Elsevier; North-Holland Publ, Amsterdam, 1991, 591-705.

[43] Material Properties; *Material Properties | Website about Elements and Materials*, (2021): http.//www.material-properties.org/ [Accessed: 21.12.2021].

[44] Goodfellow GmbH; *Material information*, (2021): http.//www.goodfellow.com/de/en-us/ catalogueinformation/material/metal [Accessed: 21.12.2021].

[45] Völkl R., Fischer B., Beschliesser M., Glatzel U.; *Evaluating strength at ultra-high temperatures—Methods and results*; Materials Science and Engineering: A 483-484, (2008), 587-589. doi:10.1016/j.msea.2006.09.171

[46] Gali A., George E.P.; *Tensile properties of high- and medium-entropy alloys*; Intermetallics 39, (2013), 74-78. doi:10.1016/j.intermet.2013.03.018

[47] Yu H., Xin Y., Wang M., Liu Q.; *Hall-Petch relationship in Mg alloys: A review*; Journal of Materials Science & Technology 34, (2018), 248-256. doi:10.1016/j.jmst.2017.07.022

[48] Xu J., Guan B., Xin Y., Wei X., Huang G., Liu C., Liu Q.; *A weak texture dependence of Hall–Petch relation in a rare-earth containing magnesium alloy*; Journal of Materials Science & Technology 99, (2022), 251-259. doi:10.1016/j.jmst.2021.04.076

[49] Somekawa H., Mukai T.; *Hall–Petch relation for deformation twinning in solid solution magnesium alloys*; Materials Science and Engineering: A 561, (2013), 378-385. doi:10.1016/j.msea.2012.10.040

[50] Caceres C.H., Mann G.E., Griffiths J.R.; *Grain Size Hardening in Mg and Mg-Zn Solid Solutions*; Metallurgical and Materials Transactions A 42, (2011), 1950-1959. doi:10.1007/s11661-010-0599-2

[51] Miracle D.B., Senkov O.N.; *A critical review of high entropy alloys and related concepts*; Acta Materialia 122, (2017), 448-511. doi:10.1016/j.actamat.2016.08.081

[52] Pickering E.J., Jones N.G.; *High-entropy alloys: a critical assessment of their founding principles and future prospects*; International Materials Reviews 61, (2016), 183-202. doi:10.1080/09506608.2016.1180020

[53] Otto F., Yang Y., Bei H., George E.P.; *Relative effects of enthalpy and entropy on the phase stability of equiatomic high-entropy alloys*; Acta Materialia 61, (2013), 2628-2638. doi:10.1016/j.actamat.2013.01.042

[54] Zhao Y.J., Qiao J.W., Ma S.G., Gao M.C., Yang H.J., Chen M.W., Zhang Y.; *A hexagonal close-packed high-entropy alloy: The effect of entropy*; Materials & Design 96, (2016), 10-15. doi:10.1016/j.matdes.2016.01.149

[55] Glatzel U., Schleifer F., Gadelmeier C., Krieg F., Müller M., Mosbacher M., Völkl R.; *Quantification of Solid Solution Strengthening and Internal Stresses through Creep Testing of Ni-Containing Single Crystals at 980 °C*; Metals 11, (2021), 1130. doi:10.3390/met11071130

[56] Inui H., Kishida K., Le L., Manzoni A.M., Haas S., Glatzel U.; *Uniaxial mechanical properties of face-centered cubic single- and multiphase high-entropy alloys*; MRS Bulletin 47, (2022), 168-174. doi:10.1557/s43577-022-00280-y